

Large-scale thermal motions of turbulent Rayleigh–Bénard convection in a wide aspect-ratio cylindrical domain[☆]

P.J. Sakievich*, Y.T. Peet, R.J. Adrian

Arizona State University, School for Engineering of Matter, Transport and Energy, Tempe, Arizona 85287-6106, USA



ARTICLE INFO

Article history:

Available online 29 June 2016

Keywords:

Rayleigh–Bénard
Turbulence
Thermal convection
Wide aspect ratio
Coherent structures

ABSTRACT

The large-scale structures that occur in turbulent Rayleigh–Bénard convection in a wide-aspect-ratio cylindrical domain are studied by means of direct numerical simulation. The simulation is performed in a 6.3 aspect-ratio cylindrical cell with a Rayleigh number of 9.6×10^7 and Prandtl number equal to 6.7. Single-point and double-point statistics compare well against experimental results under nearly identical conditions. Large-scale thermal motions with coherence times exceeding 20 eddy-turnovers (~ 600 free-fall time units) are seen in the instantaneous fields. Temporally filtering them by integrating over approximately one eddy-turnover time scale reveals a clear pattern consisting of seven discrete thermal structures: three warm, rising sectors, three cool, falling sectors and a single plume of warm, rising fluid that wanders around the center of the cylindrical cell. Smoothing over still longer times (10 and 20 eddy turn-over time scales) yields a clear hub-and-spoke pattern of warm and cool sectors in a dominantly 120° periodic pattern separated by concentrations of radial vortex lines (the spokes) plus a nearly circular plume at the center of the test section (the hub). The similarity of the patterns in the instantaneous fields and the long-time smoothed fields demonstrates long persistence of these structures, a defining characteristic of coherent structures in turbulence. The warm and cool sectors are intimately linked with conical roll-cells rotating about the spokes, and these circulations are likely the analogs of the 'wind of turbulence' found in low-aspect-ratio RBC experiments.

© 2016 The Authors. Published by Elsevier Inc.
This is an open access article under the CC BY-NC-ND license
(<http://creativecommons.org/licenses/by-nc-nd/4.0/>).

1. Introduction

Thermal convection plays an important role in many natural and engineered systems. Of the many different forms of thermal convection Rayleigh–Bénard convection (RBC) is by far the most studied (Adrian et al., 1986; Ahlers et al., 2009; Bodenschatz et al., 2000). It is one of the canonical turbulent flows, and it has been a subject of interest in the thermal turbulence community for decades. RBC occurs when a fluid between parallel, horizontal planes is heated from below and cooled from above by horizontally uniform boundary temperatures or heat fluxes. Despite this seemingly simple configuration many outstanding questions regarding the nature of turbulent RBC remain unanswered.

Recent research on RBC has focused on how the global statistics and mean profiles in small aspect-ratio cells scale throughout

the turbulent regime. Less work has been done on the characterization and life cycle of the coherent structures, despite the fact that production of turbulence by buoyancy in RBC is one of the more easily conceptualized mechanisms among all of the canonical turbulent flows. One of the most detailed descriptions of turbulent RBC structures in low aspect-ratio cells is provided by Zocchi et al. (1990). They describe five characteristic structures: plumes, thermals, waves, swirls and a large-scale circulation (LSC).

Plumes are either thermal columns or sheets that rise out of the near-wall thermal boundary layers. The sheet-like plumes have a tendency to merge when they are in close proximity to one another (Puthenveettil and Arakeri, 2005). Shishkina and Wagner (2007) performed an extensive computational study of the sheet-like plumes to provide detailed descriptions of their geometric and physical characteristics.

Thermals are transient detached packets of fluid, or blobs that ascend or descend depending upon their temperature. These structures begin as small protrusions from the near-wall viscous-conductive layer and assume a characteristic mushroom shape as they grow. Zocchi et al. (1990) also identified another structure known as swirls where the thermal emission curls back on

* This paper is dedicated to the memory of Nobuhide Kasagi, a gentleman scholar whose outstanding research and leadership served engineering and science in many important ways, including editorship of this journal.

* Corresponding author. Tel.: +1 4809650735.

E-mail address: psakievi@asu.edu (P.J. Sakievich).

itself. Models suggest that swirls arise from the same instability as thermals and plumes, but that the swirl has more shear acting in the upwind direction (Shelly and Vinson, 1992). When plumes and thermals impact the boundary layer of the opposing wallside, a wave is generated that radiates out from the center of impact. The work of Zocchi et al. (1990) shows that these waves tend to propagate toward areas where the horizontal velocities decrease and vertical velocities dominate. The regions of large vertical motion generate LSC (Qiu and Tong, 2001) which are sometimes described as "roll-cells." Aside from the waves, similar motions have been observed in relatively wide aspect-ratio ($\Gamma = \text{width}/\text{height}$) convection cells by Adrian et al. (1986) among others.

When the aspect-ratio of a convection cell is small ($\Gamma \leq 2$), a single LSC is the largest observable structure in the flow. However, when Γ exceeds roughly 4 the LSC becomes a three-dimensional, multi-roll structure as noted by du Puits et al. (2007), as well as Xia et al. (2008). This is an important observation, since the smaller scale thermals and plumes are believed to be advected horizontally by the roll-cells. Little is known about the properties of the multi-roll cell because most studies of coherent structures in RBC have been concerned with small Γ domains ($\Gamma \leq 2$).

Thus far, the most comprehensive study of Γ dependence for RBC in cylindrical domains was performed by Bailon-Cuba et al. (2010). In this work they studied how the heat transport and the LSC patterns vary as a function of Γ and Rayleigh number (Ra) at a fixed Prandtl number (Pr) of 0.7. They observed a notable difference in the heat transfer as the LSC evolves from a single roll to a multi roll state. They also observed that as Γ grows the LSC patterns favor pentagonal and hexagonal shapes. In a more recent work Emran and Schumacher (2015) estimate the time scale for the drift of these large-scale mean patterns from simulations of RBC in very wide aspect ratios ($\Gamma = 50$), but at relatively low Ra (5×10^5). Their estimate of the characteristic time scale for the large-scale drift in the very wide Γ case was on the order of 10^3 free-fall time units, well beyond the computational analysis time in their work or Bailon-Cuba et al.'s (2010) study.

The goal of this paper is to elucidate the geometrical structure and organization of LSCs in a cylindrical domain having moderately wide aspect-ratio ($\Gamma = 6.3$). This is accomplished by direct numerical simulation (DNS) using a spectral element code. Among the various methods of numerically simulating turbulent RBC we prefer DNS over RANS, LES, and hybrid RANS-LES (Chandra and Grötzsch, 2008; Kenjereš and Hanjalić, 1999; 2006; Wilson et al., 2014; Zimmermann and Groll, 2015) because the governing equations of DNS do not depend on semi-empirical parameters. We use temporal filtering on several different time-scales to extract the large, coherent structures from an otherwise chaotic turbulent field. We study a single, but representative case at $\Gamma = 6.3$, Rayleigh number = 9.6×10^7 and Prandtl number = 6.7, values that permit highly resolved DNS so detailed that the nature and organization of turbulence can be observed with accuracy throughout the entire domain. The parameters for this study were selected to facilitate direct comparison of statistics with the experiments of Fernandes (2001).

The paper is organized as follows: Section 2 presents the numerical methodology, Section 3 presents comparisons of double- and single-point statistics with the experiments of Fernandes (2001), Section 4 introduces the flow structures, Section 5 describes their organization and temporal coherence more carefully by applying temporal filters to the flow-fields, and in Section 6 we draw the conclusions.

2. Numerical methodology

Direct numerical simulation (DNS) of RBC in a cylindrical cell with an aspect-ratio ($\Gamma = \text{width}/\text{height}$) of 6.3 was performed us-

ing the spectral element code Nek5000. Nek5000 is a highly-parallelizable, well-vetted code for solving the incompressible, Navier-Stokes equations, and it currently has over 225 worldwide users (Fischer et al., 2015). The non-dimensional form of the Boussinesq equations for thermal convection is:

$$\nabla \cdot \mathbf{u} = 0, \quad (1)$$

$$\mathbf{u}_t + (\mathbf{u} \cdot \nabla) \mathbf{u} = -\nabla p + \sqrt{\frac{Pr}{Ra}} \nabla^2 \mathbf{u} + \theta \hat{z}, \quad (2)$$

$$\theta_t + (\mathbf{u} \cdot \nabla) \theta = \frac{1}{\sqrt{RaPr}} \nabla^2 \theta, \quad (3)$$

where \mathbf{u} , p and θ are velocity, pressure and temperature. Eqs. (1)–(3) were scaled spatially by the height of the cell (h), thermally by the temperature difference between the top and bottom plates (ΔT), and the velocity was scaled by the "free-fall velocity,"

$$w_f = \sqrt{hg\beta\Delta T}. \quad (4)$$

The Rayleigh (Ra) and Prandtl (Pr) numbers in Eq. (2) are defined as:

$$Ra = \frac{\beta g \Delta Th^3}{\alpha \nu}, \quad (5)$$

$$Pr = \frac{\nu}{\alpha}, \quad (6)$$

where β , g , α and ν are the coefficients of thermal expansion, gravitational constant, thermal diffusivity and kinematic viscosity respectively. The parameters of this simulation were selected to allow direct comparison with the experiments of Fernandes (2001). Fernandes conducted a series of experiments in a 6.3 Γ test cell with cylindrical side-walls. These experiments used water as the working fluid with Prandtl number ranging from 4.0 to 6.7 and Rayleigh numbers ranging from 5.8×10^7 to 1.1×10^9 . Our simulation was conducted with Prandtl and Rayleigh numbers of 6.7 and 9.6×10^7 , respectively. The simulation's boundary conditions were no-slip at all walls, constant temperature at the top and bottom plates and zero heat-flux along the side walls.

In our simulation Ra was gradually ramped from the edge of the turbulent regime ($Ra = 5 \times 10^5$) to the target Rayleigh number, and then allowed to reach a stable, fully-developed state before data was collected. The simulation was judged to be fully developed after 8 eddy-turnovers because the volume-averaged, kinetic energy in the cell began oscillating about a steady value. The eddy-turnover time for the roll-cells (t_ϵ) was estimated as the time it takes for a particle to cross the layer-depth twice:

$$t_\epsilon = \frac{2h}{\langle w_{rms} \rangle_v} \quad (7)$$

where $\langle w_{rms} \rangle_v$ is the volume-averaged, vertical, r.m.s. velocity. For reference, each eddy-turnover is roughly 30 free-fall time units (h/w_f). The DNS data used for analysis in this paper spanned approximately 20 of these eddy-turnover's, or 615 free-fall time units, and accounts for approximately 41 min in dimensional time. Brown et al. (2005) identified a random reorientation of the LSC in a unit Γ cell that occurred on a time scale of approximately 10 eddy-turnovers. Fernandes (2001) also identified coherence in the large-scale structures that met or exceeded 10 eddy-turnovers. Based off these observations $10 t_\epsilon$ was determined to be a scale of interest, and in the context of this paper it is treated as a medium, or intermediate temporal scale.

2.1. Numerical resolution

The spatial domain was discretized with hexahedral elements and a marginal amount of biasing toward the upper and lower plates was applied to the element distribution. The spectral element method (SEM) used in this simulation also applies a Gauss-Lobatto-Legendre (GLL) quadrature which clusters points inside

each element toward the boundaries and greatly improves resolution at the walls. Ninth order polynomials were used for the quadrature resulting in roughly 44 million grid points. Fernandes calculated the Kolmogorov length for this scenario to be approximately $1.2 \times 10^{-2}h$ and our simulation's grid had 5 points within this range at the wall. We also determined that this grid satisfies the spatial resolution criteria of Grötzbach (1983). The temporal resolution for each time step was approximately $t_\epsilon \times 10^{-4}$ with a corresponding CFL range of $\sim 0.6 - 0.7$.

We have conducted an a-posteriori analysis to evaluate the resolution of our results utilizing the techniques outlined by Scheel et al. (2013). Scheel et al. (2013) performed the majority of their analysis using Nek5000, and provided several specific methods for determining adequate resolution in SEM simulations of RBC (Scheel et al., 2013). One of their methods evaluates the vertical profiles of kinetic energy dissipation (ϵ) and thermal dissipation (ϵ_T) which are defined below:

$$\epsilon = \frac{1}{2} \sqrt{\frac{Pr}{Ra}} (\nabla \mathbf{u} + \nabla \mathbf{u}^T)^2 \quad (8)$$

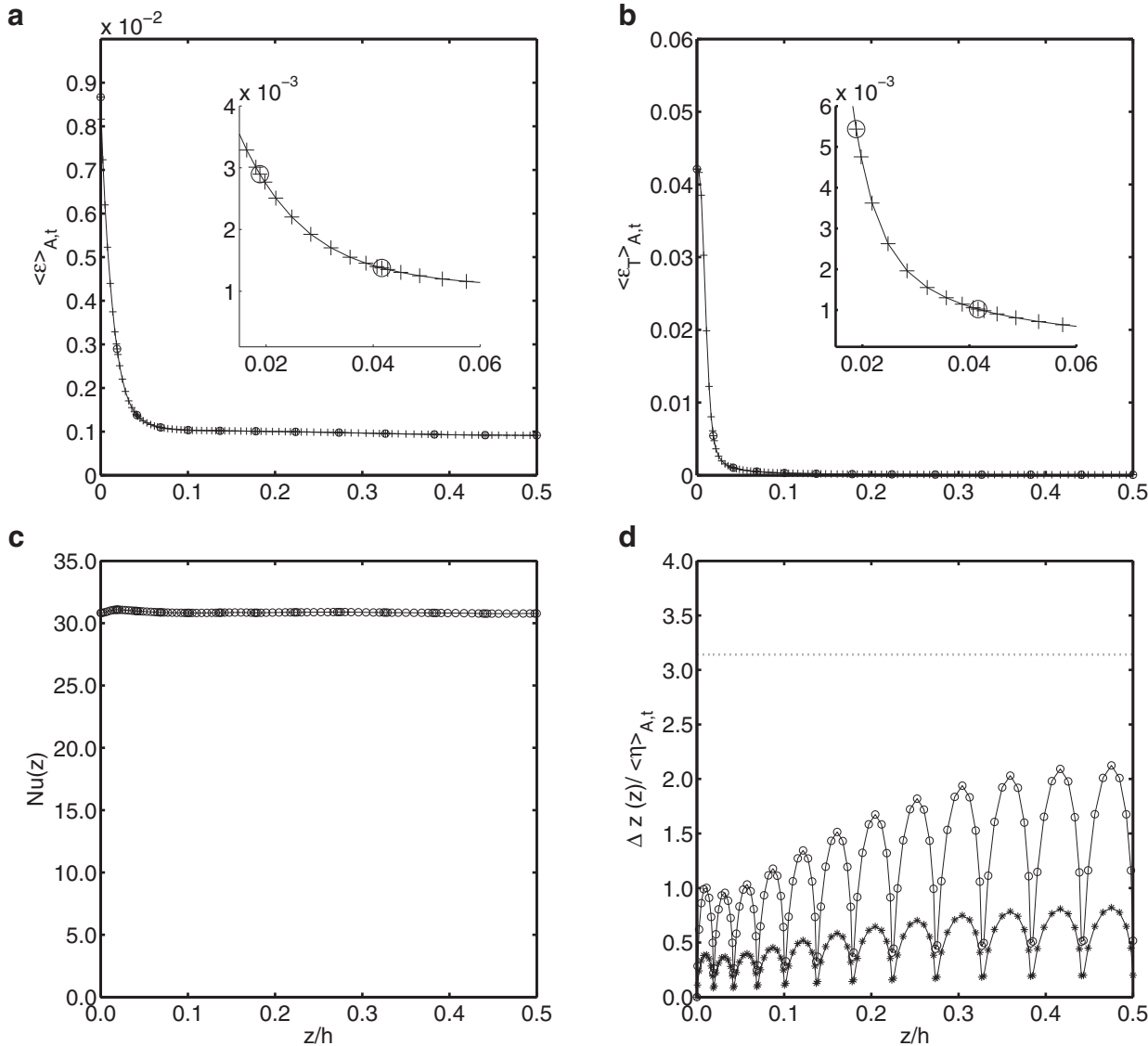


Fig. 1. Resolution tests for this simulation: kinetic energy dissipation profile (a), thermal dissipation profile (b), horizontal plane Nusselt number profile (c), vertical length scales: Kolmogorov (stars) and Batchelor (circles) (d). All time averages were calculated from 205 instantaneous snapshots with 3 free-fall times between each snapshot. Open circles in (a) and (b) are placed at the element boundary locations.

$$\epsilon_T = \sqrt{\frac{1}{PrRa}} (\nabla \theta)^2 \quad (9)$$

Profiles of these two scalar quantities are a good metric for judging convergence in SEM simulations because they are comprised of the derivatives of primary variables (\mathbf{u}, θ). SEM results are guaranteed to be C0 continuous, or continuous in the primary variables, within the elements and across element boundaries. The derivatives of these terms, or secondary variables are guaranteed to be continuous within the elements, but not across element boundaries (Deville et al., 2002). Thus, discontinuities in the derivatives across element boundaries are commonly used to detect under-resolved simulations. Profiles for both dissipation terms are presented in the top two panels of Fig. 1. To illustrate smoothness and continuity of the present computations, the dissipation profiles and element boundaries are shown in the near-wall region, where the gradients are largest. These profiles were generated through area and time averages in the same manner as Scheel et al. (2013). The smoothness of the dissipation profiles testifies that the simulations are well resolved according to this criterion.

Table 1

Nusselt number calculations in row order: average planar Nusselt number ($\bar{Nu}(z)$) and the associated standard deviation, Nu at the bottom plate, Nu at the top plate, Nu from volume averaged kinematic heat flux, Nu from volume averaged kinematic dissipation, Nu from volume averaged thermal dissipation.

$\langle \bar{Nu}(z) \rangle_z \pm \sigma$	Nu_{bot}	Nu_{top}	Nu_{Q_b}	Nu_ϵ	Nu_{ϵ_T}
30.89 ± 0.08	30.83	30.85	30.87	30.83	30.12

Another methodology, initially proposed by [Bailon-Cuba et al. \(2010\)](#) and utilized by [Scheel et al. \(2013\)](#), is to define height dependent Kolmogorov (η_K) and Batchelor (η_B) scales by averaging over horizontal planes and time.

$$\langle \eta_K(z) \rangle_{A,t} = \frac{Pr^{3/8}}{Ra^{3/8}} \langle (\epsilon(z)^{-1/4}) \rangle_{A,t} \quad (10)$$

$$\langle \eta_B(z) \rangle_{A,t} = \frac{1}{Pr^{1/8} Ra^{3/8}} \langle (\epsilon(z)^{-1/4}) \rangle_{A,t} \quad (11)$$

From here the original Grötzsch criterion can be modified to the following ([Bailon-Cuba et al., 2010; Scheel et al., 2013](#)):

$$\frac{\Delta z(z)}{\langle \eta(z) \rangle_{A,t}} < \pi \quad (12)$$

where $\Delta z(z)$ is the vertical grid spacing and η is either the Batchelor or Kolmogorov scale. We have plotted this criterion for both the Kolmogorov and Batchelor scales in the lower right panel of [Fig. 1](#) where it can be seen that we are adequately resolved according to this criterion.

The final resolution criterion that we wish to comment on is convergence of the Nusselt number which can be defined on individual planes ([Eq. \(13\)](#) below), by volumetric averaging of the kinematic heat flux ([Eq. \(14\)](#) below), or by balancing dissipation inside the convection cell ([Eqs. \(15\)](#) and [\(16\)](#) below) [Scheel et al. \(2013\)](#).

$$Nu(z) = \sqrt{RaPr} \langle w\theta \rangle_{A,t} - \frac{\partial \langle \theta \rangle_{A,t}}{\partial z} \quad (13)$$

$$Nu_{Q_b} = 1 + \sqrt{RaPr} \langle w\theta \rangle_{V,t} \quad (14)$$

$$Nu_\epsilon = 1 + \sqrt{RaPr} \langle \epsilon \rangle_{V,t} \quad (15)$$

$$Nu_{\epsilon_T} = \sqrt{RaPr} \langle \epsilon_T \rangle_{V,t} \quad (16)$$

$Nu(z)$ is plotted in the lower left panel of [Fig. 1](#), and a summary of the different calculations of Nu is included in [Table 1](#). These results show that we have good agreement between the different methodologies for computing Nu and that the majority of these methodologies give a Nu within 0.2% of each other. The only outlier is Nu_{ϵ_T} which is about 2.5% lower than the others.

3. Comparison with experiments

This section compares two-point and single-point statistics computed from the DNS data with the corresponding quantities found in the experiments of [Fernandes \(2001\)](#). Quantitative comparisons of the velocity and temperature fields of RBC simulations and experiments have been rare to date, and we hope that the present comparison and discussion will provide useful guidelines for future studies. The agreement one should expect from this comparison is tempered by certain differences inherent to DNS and experiment, despite our best efforts to numerically recreate the environment of Fernandes' experiment. First, DNS yields data from every grid point in the domain, but over a temporal duration that is limited by the cost of computation. In contrast, experiments yield data from a limited subset of points in the volume, but they can be performed over very long durations. These factors lead to different time averaging protocols. Second, differences

Table 2

A select list of RBC DNS studies. Total averaging times are listed in the 4th column.

Group	$O(Ra)$	Pr	Free-fall times	Γ
Kerr (1996)	10^7	0.7	116	6.0
Shishkina and Thess (2009)	$10^8 - 10^9$	4.38	290	1.0
Bailon-Cuba et al. (2010)	$10^7 - 10^9$	0.7	$\sim 80 - 300$	0.5–12.0
Scheel et al. (2012)	$10^5 - 10^8$	0.7	~ 480	1.0
Scheel et al. (2013)	$10^6 - 10^9$	0.7	~ 75	1.0 and 3.0
Emran and Schumacher (2015)	10^5	0.7–10	~ 600	50
Current work	10^8	6.7	615	6.3

between the data sampling domains and assumptions concerning horizontally homogeneous statistics lead to different spatial averaging protocols. Third, the experimental and DNS data were non-dimensionalized using different, albeit related scales for velocity and temperature. Fourth, although both flow fields occur in geometrically similar cylindrical domains with constant temperature horizontal boundaries, differences exist between the ideal, mathematically perfect boundary conditions of the DNS and the realistic, imperfect thermal boundary conditions of the experiment.

3.1. Differences between experimental and numerical data collection protocols

In the following sections we discuss the foregoing differences and the steps taken to minimize their effects on the statistical comparison.

3.1.1. Differences in temporal averaging

[Fernandes' \(2001\)](#) statistics were generated from a set of 300 statistically independent snapshots which were obtained over very long averaging times. These snapshots were collected in groups of 15 with $4z*/w^*$ (~ 30 –40 s) between each snapshot in a group ($z_* = 0.5h$ is half the layer depth, w^* is the Deardorff velocity scale precisely defined later). The heat source was periodically turned off for 30 min to an hour between sets of snapshots, then turned back on and allowed to settle for 4–12 h. This perturbing of the flow was done to keep the large-scale-motions from developing any preferential direction. The data between the perturbations was treated as independent realizations of the order of $O(1000)$ free-fall times in duration and resulted in an averaging procedure that included temporal and ensemble averaging.

At each Ra the total procedure took hundreds of hours which is $O(10^5)$ free-fall time units. Recreating a DNS data set that spans a similar amount of time and/or incorporates a similar number of realizations would be prohibitively expensive. For comparison, [Table 2](#) displays the total runtimes of a selection of the representative numerical simulations in RBC to illustrate this wide gap. The next section illustrates how the additional spatial data available through DNS can help narrow this gap.

3.1.2. Differences in spatial dimensions

As previously mentioned, we designed our DNS to match the experiments of [Fernandes \(2001\)](#) as close as possible, and we define the spatial domain for both studies in cylindrical coordinates as Ω_F .

$$\Omega_F(r, \phi, z) : r \in 0 : 3.15h; \quad \phi = 0 : 2\pi; \quad z \in 0 : h \quad (17)$$

However, Fernandes did not utilize the entire volume for his velocity measurements. Instead, he chose to take measurements in the center of Ω_F far enough from the side walls so he could apply the assumption of horizontal homogeneity to the velocity statistics ([Fernandes, 2001](#)). Fernandes obtained velocity measurements through the use of two-dimensional, particle image velocimetry (PIV) at a vertical plane in the center of the cell with a field of

view $1.85h$ in length and h in height. We shall refer to this as the experimental window Ω_E .

$$\Omega_E(r, \phi, z) : r \in 0 : 0.925h; \quad \phi = 0, \pi; \quad z \in 0 : h \quad (18)$$

One notable advantage that our DNS data set has over the experimental results of Fernandes is a third spatial dimension from which to draw data. [Fernandes \(2001\)](#) applied horizontal-line averages on his 2D PIV data sets to examine the velocity statistics in the plane Ω_E . To utilize the extra dimension in the DNS results we defined a sub-volume within Ω_F that can be generated by rotating Ω_E about the central axis:

$$\Omega_{SV}(r, \phi, z) : r \in 0 : 0.925h; \quad \phi = 0 : 2\pi; \quad z \in 0 : h \quad (19)$$

We then projected the instantaneous DNS results within Ω_{SV} onto evenly spaced points in cylindrical coordinates, and performed horizontal, planar averages to the data to mimic the line-averaging performed by Fernandes. For example, the mean vertical velocity averaging procedure we used in Ω_{SV} is defined as follows:

$$\langle w(z) \rangle_{A,t} = \frac{1}{N_T N_P} \sum_{i=1}^{N_T} \sum_{j=1}^{N_P} \frac{2r_j}{R} w(r_j, \phi_j, z_j, t_i) \quad (20)$$

where N_T is the number of instantaneous snapshots in time, N_P is the number of points in the plane, the subscript A stands for the “area-averaged”, and $R = 0.925h$ is the radius of a circular cross-section of Ω_{SV} . We also collected statistics along horizontal planes that spanned the full DNS domain (Ω_F) using numerical averaging procedures native to Nek5000.

Another notable difference in the DNS and experimental data sets is in the horizontal velocity components. The DNS calculations were performed in cartesian coordinates where u and v correspond to the x and y axis. However, the domain is cylindrical and so cartesian velocity components do not properly reflect the periodicity found in the cylindrical domain. Additionally, since Fernandes collected 2D velocity fields in a plane intersecting the central axis of Ω_{SV} the horizontal component in his data sets can be interpreted as a radial velocity component. Based on these two observations we chose to compare radial velocity statistics from the DNS with the horizontal velocity statistics Fernandes published. The DNS radial velocity component (u_r) was extracted from the two horizontal velocity components using the simple transformation in [Eq. \(21\)](#).

$$\begin{aligned} \phi &= \tan^{-1}(x/y) \\ u_r(x, y, z, t) &= u(x, y, z, t) \cos \phi + v(x, y, z, t) \sin \phi \end{aligned} \quad (21)$$

In the remainder of the paper, radial velocity will be implied for our DNS results whenever horizontal velocity is referred to.

3.1.3. Differences in scaling

It should be noted that Fernandes non-dimensionalized variables using the Deardorff scales of velocity and temperature ([Deardorff, 1970](#)), and a vertical length equal to one-half the layer depth ($z_* = 0.5h$). The excellent scaling properties of Deardorff's scales have been shown to collapse, to within $\pm 15\%$, the profiles of second and third order turbulence moments measured in laboratory experiments at $Pr = 6.8$, $Ra = 10^7$ onto atmospheric measurements of convective boundary layers at $Pr = 0.7$ and $Ra \sim 10^{14} - 10^{16}$ by [Adrian et al. \(1986\)](#). Correlation of the scaled data over such a huge range is testimony to the power of this scaling. Moreover, the non-dimensional variables are $O(1)$, indicating that the scales themselves are representative of the physical variables. The Deardorff velocity and temperature scales are defined below, where Q_o is the kinematic heat flux whose units are [$K \cdot mm/s$]. Q_o can be determined by dividing the standard heat flux at the wall (H_0 [W/mm^2]) by the density (ρ [kg/mm^3]) and specific heat (c_p [$J/(kg \cdot K)$]).

$$Q_o = H_0 / (\rho c_p) \quad (22)$$

$$w^* = (\beta g Q_o h)^{1/3} \quad (23)$$

$$\theta^* = \frac{Q_o}{w^*} \quad (24)$$

However, the DNS procedure used the “free-fall” scales during the calculations because they provide better accommodation for the constant temperature boundary conditions. To provide a one-to-one comparison of velocity statistics with Fernandes and to take advantage of the compelling properties of Deardorff scales discussed above, all computational velocity data presented in this paper was rescaled to the Deardorff scales. This was accomplished by multiplying the DNS field by w_f and then dividing by w^* . w^* was determined by calculating Nu in the simulation and then scaling it against Fernandes values of Nu and w^* at this Ra (9.6×10^7). These were $Nu = 27.9$ and $w^* = 2.5$ mm/s, respectively ([Fernandes, 2001](#)).

The simulated value of Nu for $Ra = 9.6 \times 10^7$ (see [Table 1](#)) was approximately 10% higher and lead to $w^* = 2.6$ mm/s. Our simulation shows well converged results (see [Section 2.1](#)), and Fernandes demonstrated that heat loss through the side walls was kept to under 2% for his experiments ([Fernandes, 2001](#)), so it seems that the usual suspects of insufficient numerical resolution and heat loss through the side walls are not to blame. One possible culprit for the discrepancy in Nu is the differences between experimental and numerical boundary conditions. The no-slip velocity boundary conditions were identical between the two cases, but the thermal boundary conditions were not. The numerical simulation explicitly enforced constant temperature boundaries while the experiment maintained an average constant heat flux through resistive heaters. Additionally, the simulation provided sidewalls that are perfectly insulated while the experiment had sidewalls with finite thermal conductivity.

3.2. Statistics results

3.2.1. Two-point statistics

In this section the two-point correlation functions of the velocity field for vertical separation are compared against the published results of Fernandes in [Fig. 2](#). This statistic is a useful mechanism for analyzing similarity in the spatial structure of the velocity field, and it is a good metric to judge how the organization of our DNS velocity field compares with the experiment's.

Visual inspection of [Fig. 2](#) shows the contour shapes and amplitudes between the results are qualitatively in good agreement. This indicates that the large-scale velocity structure in the numerical field matches the experiment within the specified sub-volume Ω_{SV} . The two-point correlation does not tell us that the velocity structures have the same azimuthal orientation or vertical direction, but rather that their shape and size are very similar. We note that in the DNS contours the horizontal velocity correlations are slightly larger at the vertex (2,2) and the experimental results are slightly larger around the origin (0,0). We also observe a similarity in the shape of the contours at the opposing corners in the experimental and DNS plots. This indicates that the DNS' horizontal velocity structure within Ω_{SV} is similar to a reflection across the mid-plane of the velocity structure observed in the experiments. A more quantitative comparison of velocity statistics is provided through the single-point statistics in the next section.

3.2.2. Single-point statistics

In this section the single-point vertical and horizontal velocity statistics as well as the temperature fluctuations are compared against those of [Fernandes \(2001\)](#). Separate profiles are presented for DNS statistics that are averaged on horizontal planes that span the sub-volume Ω_{SV} and the entire volume Ω_F . We also note that

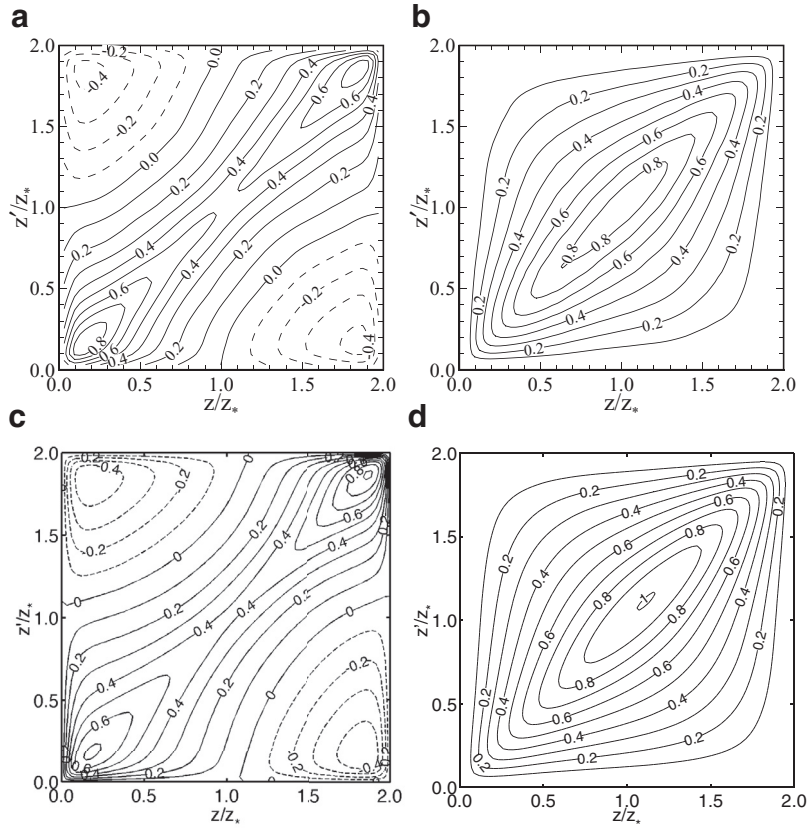


Fig. 2. Contour plot of the vertical, two-point correlation of the u-velocity component (left) $\langle u_r(z)u_r(z') \rangle_{A,t}$ and w-velocity component $\langle w(z)w(z') \rangle_{A,t}$ (right), all values normalized by w^2 : (a) and (b) experimental results at $Ra = 2 \times 10^8$ (averaged within Ω_F) ($Ra = 2 \times 10^8$ is the closest Ra to our simulations, for which two-point correlation is presented in the experiments), (c) and (d) DNS at $Ra = 9.6 \times 10^7$ (averaged within Ω_{SV}).

the r.m.s velocity profiles in this section are the full velocity components, and not the fluctuations. This was done to match the results of [Fernandes \(2001\)](#) who assumed a zero-mean velocity field for his r.m.s. calculations.

[Fig. 3](#) displays the mean and r.m.s. profiles for the vertical velocity component. The r.m.s vertical velocity profile within Ω_{SV} over predicts the magnitude by $\sim 11\%$ when compared to the experimental results. This over prediction is based on a pointwise comparison between the numerical results and a profile interpolated between the experimental data sets at $Ra = 5 \times 10^7$ and 2×10^8 to the DNS Ra number. Additionally, a notable bias is present in the upper half of the numeric profile. However, when the horizontal averaging is extended to span all of Ω_F the profile's symmetry about the mid-plane improves and the profile's magnitude reduces to within 5% of the expected value. A similar trend is seen in the mean vertical velocity profiles.

The mean vertical velocity profile from sampling points within Ω_{SV} is dramatically larger than if averaged over the full domain Ω_F (which is identically zero as expected). It is also larger than the experimental profiles which were averaged over Ω_E , and it has a sign difference. The difference in sign between the experimental and numerical results we attribute to the lack of preferred direction in RBC systems. There is nothing in the geometry, boundary conditions or governing equations to give preference to a positive or negative vertical velocity making up-drafts and down drafts of equal probability in the LSC. The sign difference between the experimental and numerical profiles suggests that while our DNS results clearly indicate a central up-draft, a central down-draft has likely prevailed in the experiments. This sign difference is also consistent with the reflection of structure we observed in the two-point correlations for the horizontal velocity components ([Fig. 2](#)).

The trends in r.m.s. horizontal velocity profiles in [Fig. 4](#) are similar to the trends in vertical velocity profiles. The r.m.s profile from within Ω_{SV} is slightly larger than the profile averaged across the entire domain, but both of these profiles are very close to the experimental results at similar Ra . We also see a continuation of the reflection for the horizontal velocity structure that was observed in the two-point statistics. The experimental profiles have slightly larger peaks near the lower boundary, and the numerical profiles have larger peaks toward the top boundary. This follows the trend seen in [Fig. 2](#) and supports our observations regarding the vertical profiles displayed in [Fig. 3](#).

The mean horizontal velocity profiles have a slightly different behavior than their vertical velocity counterparts. Inside Ω_{SV} the mean takes a similar shape and direction when compared to the experimental profiles. The mean inside Ω_{SV} is notably larger in magnitude than the expected profile that lies between experimental profiles at $Ra = 5 \times 10^7$ and 2×10^8 in the upper half of the domain ($z/h \geq 0.5$), and the overshoot is similar in magnitude to the mean vertical velocity profile in [Fig. 3](#). When the horizontal averaging is extended to span Ω_F the mean horizontal profile changes direction and substantially reduces in magnitude. We attribute this change to the organization of the LSC in the moderately large Γ domain. This structure will be reviewed extensively in the next section.

Finally, we present statistics from the temperature field in [Fig. 5](#). Fernandes did not provide mean temperature profiles to compare against, but the slightly higher bulk temperature in the Ω_{SV} mean profile is consistent with the mean, vertical velocity profile from [Fig. 3](#). This indicates a net updraft of warm fluid within Ω_{SV} . When the horizontal averaging is extended to the entire domain the mean profile's bulk temperature value returns to

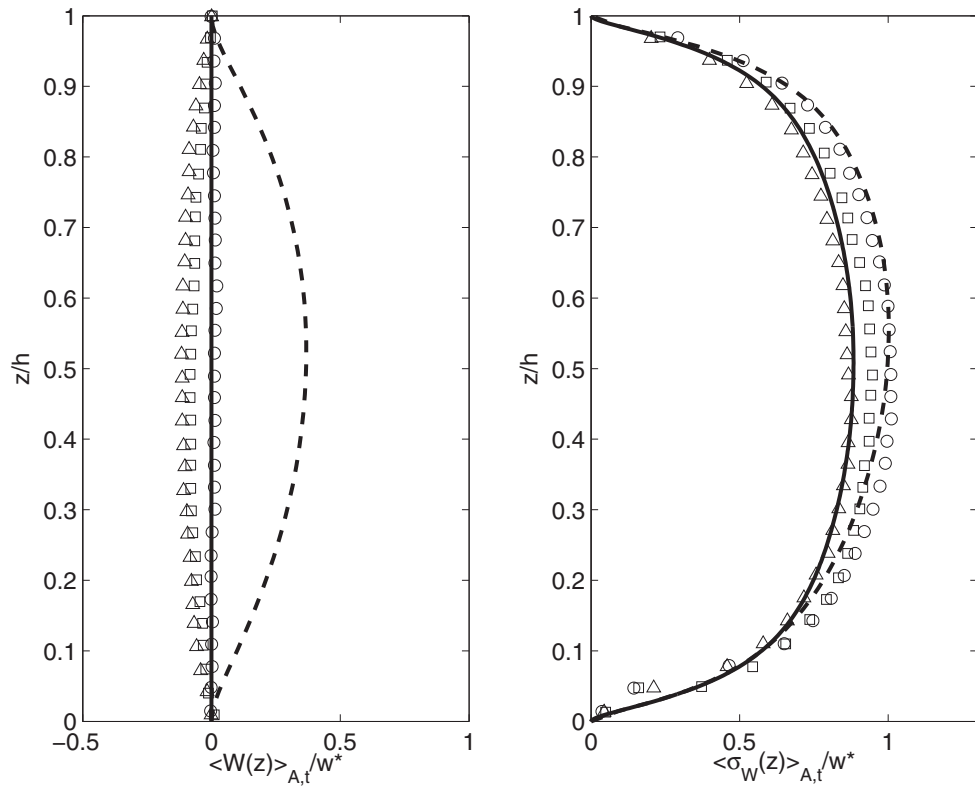


Fig. 3. Ensemble and horizontally averaged mean (left) and r.m.s. (right) vertical velocity profile normalized by w^* : DNS: $Ra = 9.6 \times 10^7$, averaging domain Ω_F (—) and averaging domain Ω_{SV} (---); Experiment: $Ra = 6 \times 10^7$ (Δ), $Ra = 2 \times 10^8$ (\square), $Ra = 1 \times 10^9$ (\circ).

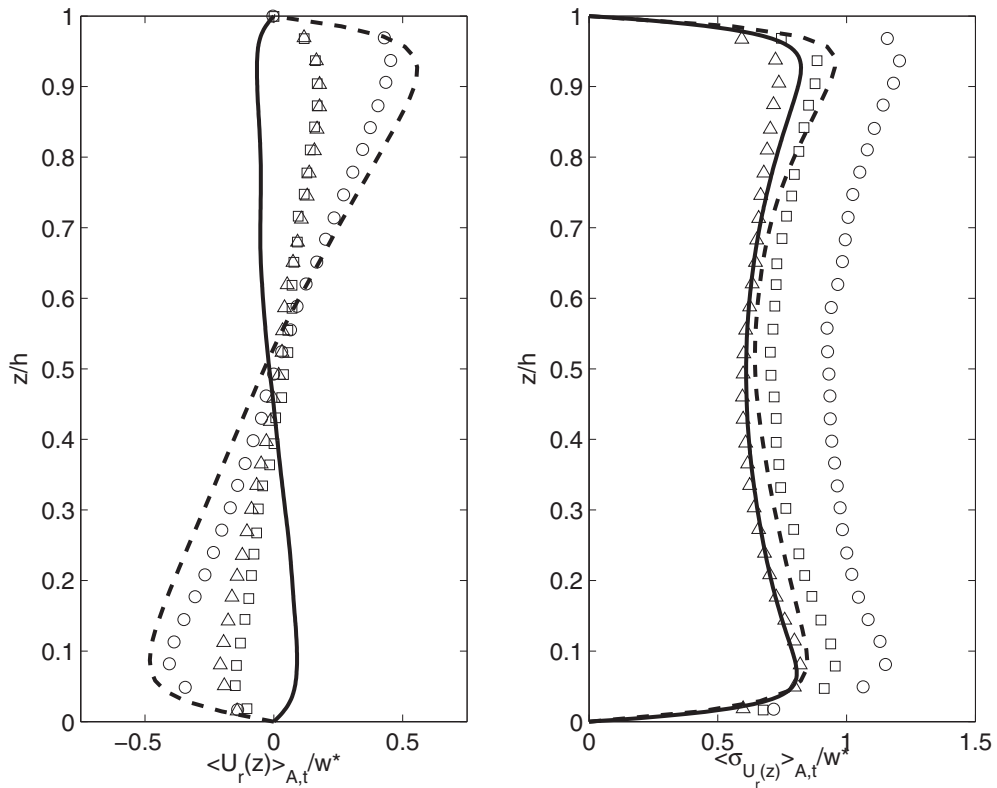


Fig. 4. Ensemble and horizontally averaged mean (left) and r.m.s. (right) horizontal velocity profiles normalized by w^* : DNS: $Ra = 9.6 \times 10^7$, averaging domain Ω_F (—) and averaging domain Ω_{SV} (---); Experiment: $Ra = 6 \times 10^7$ (Δ), $Ra = 2 \times 10^8$ (\square), $Ra = 1 \times 10^9$ (\circ).

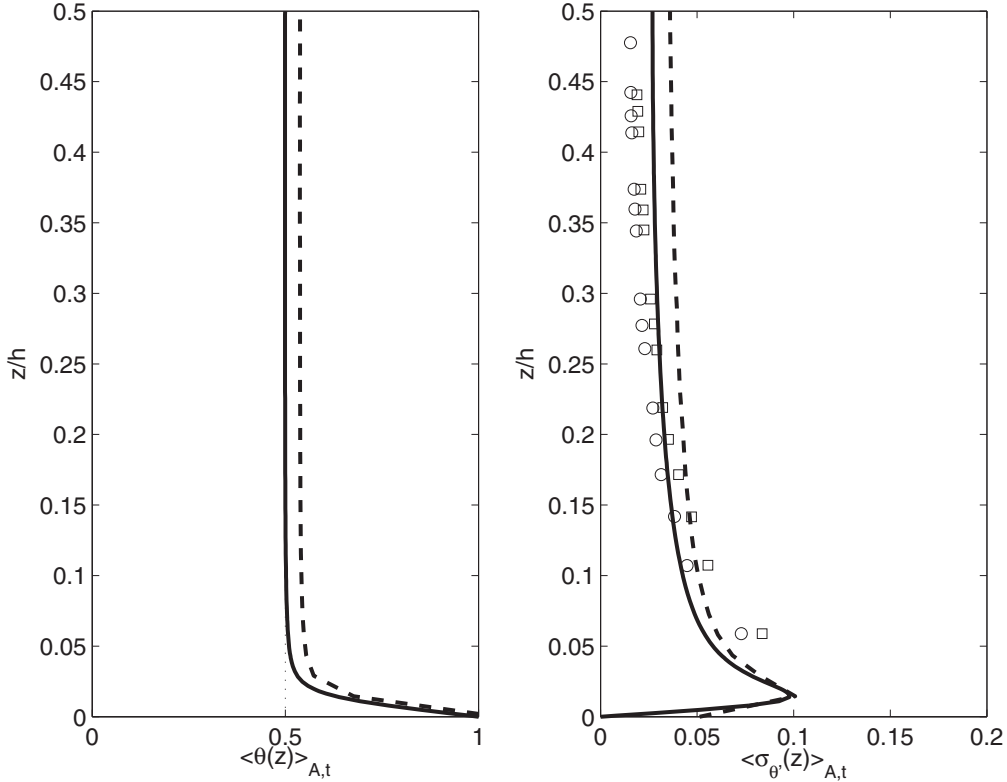


Fig. 5. Ensemble and horizontally averaged mean temperature profile (left) and r.m.s temperature fluctuations (right) normalized by ΔT : DNS: $Ra = 9.6 \times 10^7$, averaging domain Ω_F (—) and averaging domain Ω_{SV} (- -); Experiment: $Ra = 2 \times 10^8$ (□), $Ra = 5 \times 10^8$ (○).

the expected value of 0.5 outside of the thermal boundary layer. The r.m.s. profiles for the temperature fluctuations are consistent with this interpretation, and the simulated r.m.s. profiles display slightly larger magnitudes than experimental profiles in the bulk of the flow, corresponding to a preferential central up-draft (higher temperatures) in the simulations as opposed to a probable slight down-draft (lower-temperatures) in the experiments.

Overall, we find that the statistics from our simulation compare well with the experimental results of Fernandes. We see good agreement in shape, direction, and magnitude for the various profiles despite only having a single realization of the flow field and a much smaller averaging time. The profiles tend to have larger magnitudes when they are constructed from averages within Ω_{SV} . However, when the averaging domain is increased to span Ω_F the profiles are, for the most part, within $\pm \sim 5\%$ of the experimental results.

4. Structure of the flow

The remainder of the paper focuses on analyzing the large-scale thermal structures and their relationship to the pattern of the large-scale circulation. Fig. 6 displays several cut planes of the instantaneous temperature field. The color scale of the temperature field spans $\pm 5\%$ of ΔT to highlight the structures within the bulk region where the large-scale structures reside.

Large concentrated areas of warm and cool fluid can be discerned in the instantaneous temperature field on the horizontal plane in Fig. 6. The vertical planes in Fig. 6 show that the warm and cool regions consist of concentrations of smaller structures (plumes and sheets) crossing the bulk layer. The mid-plane is a favorable location to investigate structures that span the entire layer depth because the mean horizontal velocity components are minimal, and the up (warm thermal) and down (cool thermal) motions have comparable strength due to symmetry about the mid-plane.

Fig. 7 shows a more detailed view of the mid-plane to better illustrate the concentrated thermal areas. The left panel is from the same time instance displayed in Fig. 6, and the right panel displays results $5.9 t_\epsilon$ (117 free-fall times) later to illustrate that these thermal concentrations can be observed for extended periods of time. The similarities between these two instances suggest that an underlying large-scale structure exists, but it's hard to discern the structures precise form with such a high level of noise from the background turbulence.

5. LSC extraction by smoothing in time

In the following section we use running, temporal averages to filter noise from the flow field and reveal properties about the large-scale structures for relatively large Γ , turbulent RBC. This averaging procedure smooths the signal and it is defined as:

$$\langle u(x, y, z) \rangle_t = \frac{1}{T} \int_{t_0}^{t_0+T} u(x, y, z, t) dt \quad (25)$$

where T is the averaging period or filter width, and t_0 is the starting point in time for each filtering operation. In this section we will use the terms "averaging," "filtering" and "smoothing" interchangeably since the purpose of our running average procedure is to remove small scale fluctuations and preserve the larger scale structures who have longer life cycles.

5.1. Short-time filtering ($T=1 t_\epsilon$)

When the temperature field is averaged over a period of $1 t_\epsilon$ seven discrete thermal concentrations begin to emerge. These large-scale thermal structures can be identified by studying the left panel of Fig. 8. Six of the seven thermals are connected to the cell's side walls, and are alternately arranged by temperature. The seventh thermal is a warm updraft located in the central region of the

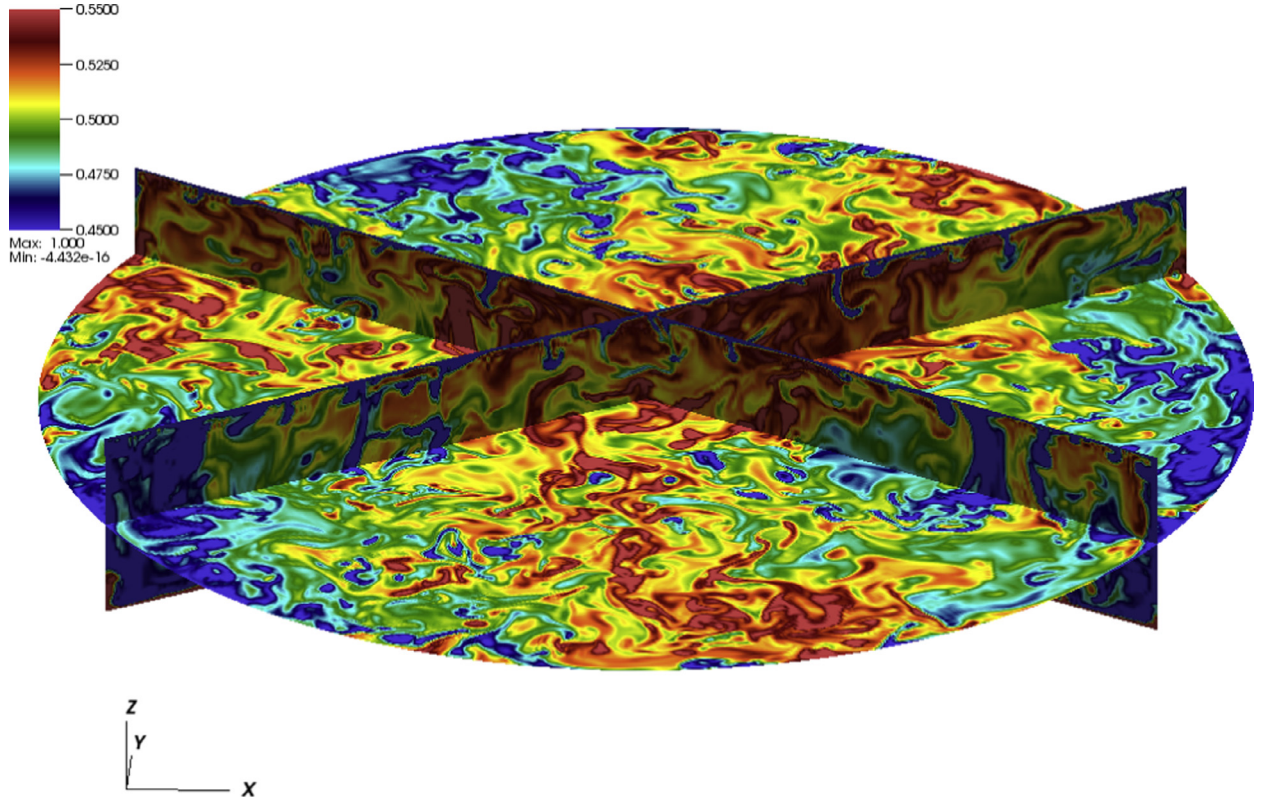


Fig. 6. Instantaneous temperature data scaled between 0.45 and $-0.55\Delta T$ at the horizontal cut plane at $z/h = 0.5$ and vertical cut planes at 30° , 150° from the x -axis. (For interpretation of the references to color in this figure, the reader is referred to the web version of this article).

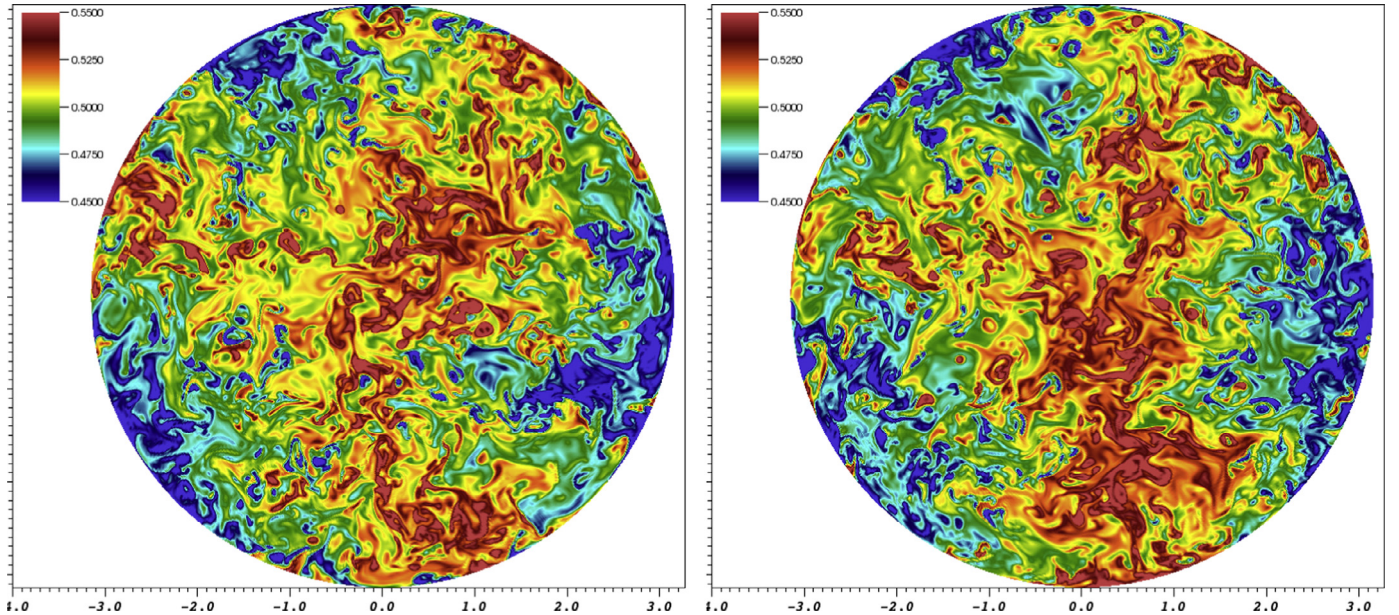


Fig. 7. Instantaneous temperature data in the $x-y$ plane at $z/h=0.5$ for two different time instances $5.9t_e$ apart.

cell, but noticeably off center. A significant portion of the central thermal resides within the volume where we collected the sub-domain statistics (Figs. 2–5). This central thermal structure partially explains the differences between statistics in the sub-domain (Ω_{SV}) and those that spanned the entire domain (Ω_F) because it would create a bias for warm fluid and up flow within Ω_{SV} .

Coupling between the large-scale thermal field and the velocity roll-cells is illustrated by comparing the spatial locations of the mean velocity up/down drafts and the vector field connecting

these drafts. The right panel in Fig. 8 displays the vertical velocity component at the mid-plane to illustrate the location of the mean vertical drafts, and a vector field at the plane $z = 0.92h$, corresponding to the local maxima in the mean horizontal velocity profile (Fig. 4), to show how the drafts are interconnected by flow near the boundaries. A comparison of the left and right panels in Fig. 8 clearly shows that the warm thermals represent velocity sources and the cool thermals represent velocity sinks from the top-down perspective. Connecting the warm and cool thermals

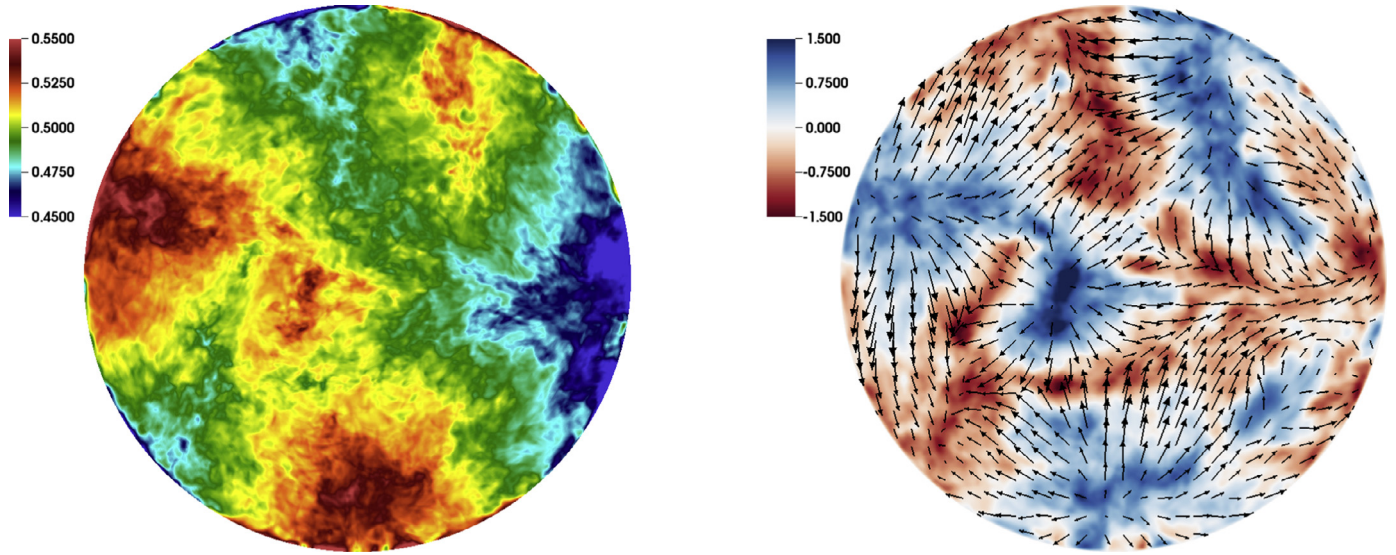


Fig. 8. Thermal field at the mid-plane scaled from 0.45 to $0.55\Delta T$ (left); vertical velocity field at the mid-plane scaled between -1.5 and $1.5 w^*$ with velocity vectors in the $x-y$ plane at $z/h=0.92$ superimposed (right); all results are time averaged over the 1st t_ϵ of data.

creates a complete roll-cell. This basic method can be used to conceptualize the 3D multi-roll-cell pattern in a simple and intuitive manner.

The short-time-averaged temperature fields in Fig. 9 can be used to interpret the fluctuation level still present in the large-scale structures after the short-time averaging. These instances were taken $3 t_\epsilon$ apart to increase the dynamic effect through static visualizations. Very little change is observed in the thermal field which shows that the large-scale thermals are relatively stationary over the averaging time of this data set. The up and down drafts near the walls show little change in spatial location, however there is some noticeable fluctuation in their individual sizes.

Qualitatively, we observe the central thermal in Fig. 9 moving from left to right during the time series. It is difficult to be certain if the structure is approaching a steady state, or if a secondary fluctuation with even slower dynamics is dominating the flow. However, we can be certain that the smoothing from this short time average does not bring the field to a steady state, and that a pattern of seven large-scale thermals is persistent across the entire range of our data set.

5.2. Medium-time filtering ($T=10 t_\epsilon$)

In this section we increase our averaging time to $10 t_\epsilon$ (300 free-fall times) to smooth out the fluctuations that were still present after short-time averaging. This "medium" averaging time is effectively half of our data set resulting in two instances to observe, see Fig. 10.

The results in Fig. 10 show a striking set of triangular patterns for the large-scale thermal field that are manifest at the mid-plane. The seven discrete thermals that were identified in the previous section have clearer boundaries and are now visibly obvious. From Fig. 10 we see the emergence of a dominant low order mode with 120° , azimuthal periodicity. There are several interesting departures from pure periodicity that can be observed in medium-time average data such as the central thermal residing off the central axis and the size variation amongst the thermals along the outer wall. The significant change in the central thermal location between the two panels in Fig. 10 illustrates that the central plume still moves around the center at these time scales.

However, the large-scale organization that is revealed through $10 t_\epsilon$ of temporal smoothing is similar for both instances. Fig. 11

illustrates how the large-scale organization can be interpreted as a hub and spoke pattern with roll-cells forming between alternating thermals around the outer wall and vortex lines located between the thermals. The central, uprising thermal creates in-plane, azimuthal vorticity due to the shearing effects, manifested as a circular vortex ring around it. This vorticity acts to reinforce the interaction of the large-scale thermal with the side thermals of opposing temperature and to strengthen the global large scale motions observed in the simulations.

The right panels in Figs. 10 and 11 represent a symmetric pattern, the one which will also likely persist over longer averaging times. The left panels in Figs. 10 and 11 illustrate the strong effect the central thermal can have on the velocity structure. When the location of the central thermal moves off the center axis it comes closer to two other thermals with similar temperatures. This shift breaks some of the symmetry, enhances the interaction between the central thermal and the nearest thermals of opposing temperature, and can cause the other two vortex lines to break and reform as drawn in the left panel of Fig. 11.

To test the validity of the concepts presented in Fig. 11 we computed the in-plane vorticity at the mid-plane for each of these realizations and the results are displayed in Fig. 12. The lines of vorticity in Fig. 12 verify that the spokes in the temperature field between large-scale thermals are indeed regions of strong vorticity, and that the central thermal has a vortex encircling it which interacts with the spokes. These similarities give weight to the conceptual basis of the right hand diagram in Fig. 11. However, the conceptual diagram fails to replicate the fact that the warm regions are narrower than the cool regions. This can be remedied by recognizing that the width of the vortex loops need not be equal, which would amount to squeezing of the vortex lines closer to the warm thermals (because the central thermal is an updraft) that reside in the outer region of the convection cell, in the right diagram of Fig. 11.

It is recognized that the pattern of large scale motions is most likely a function of Γ and that additional patterns may exist at other Γ 's and in other domains. However, there is a strong resemblance between the pattern in the left panel of Fig. 10 and the pattern shown by Bailon-Cuba et al. (2010) at similar values of Γ and Ra even though Pr was smaller by a factor of 10. During the initialization stage of this simulation we incrementally increased Ra and allowed the initial transients to settle after each discrete jump

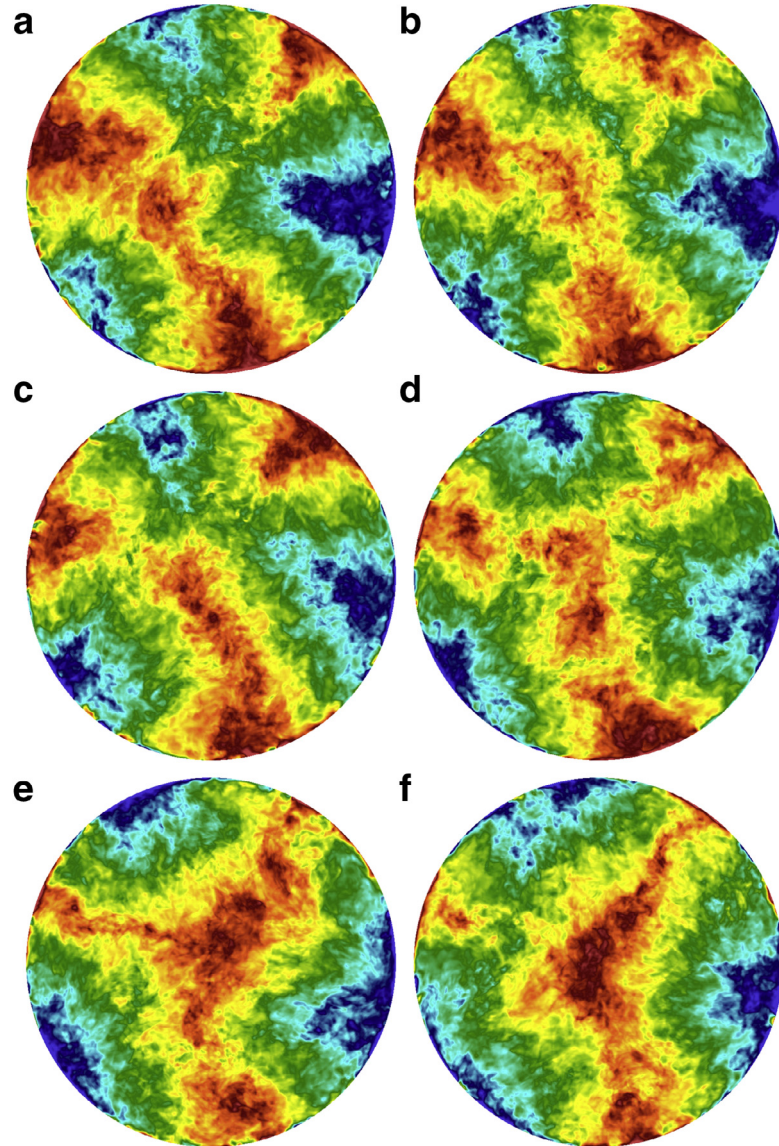


Fig. 9. Temperature field averaged over one t_ϵ at $t_0 = 2 t_\epsilon$ (a), $5 t_\epsilon$ (b), $8 t_\epsilon$ (c), $11 t_\epsilon$ (d), $14 t_\epsilon$ (e), and $17 t_\epsilon$ (f) in the $x - y$ plane at $z/h = 0.5$ scaled between 0.45 and 0.55 ΔT , the color panel is the same as in Fig. 8 (left). (For interpretation of the references to color in this figure legend, the reader is referred to the web version of this article).

in Ra . During this process we qualitatively observed a transition in the large-scale thermals organization from a pattern that is more indicative of a single roll cell to the multi-roll cell state we have presented. From this we speculate that the characteristic size of the large-scale thermals will vary with Ra ; however, this concept warrants a more thorough investigation.

5.3. Long-time filtering ($T=20 t_\epsilon$)

We conclude our investigation of the large-scales structures at moderately large Γ by evaluating the full time averaged field from our DNS data set. Fig. 13 provides a time average over the complete $20 t_\epsilon$. Fig. 13(a) displays multiple cut planes of the average field to show the level of symmetry of the structure. The angles of the 3 vertical cut planes were chosen in an attempt to maximize intersection between large-scale thermals that are positioned directly across from one another in the cell. We observe that thermals directly across from one another are not perfectly aligned. Careful observation of Fig. 13(b) will show that the central thermal is still not completely centered in the cell, and that the outer thermals

are still not uniform in size. However, the dominance of the 120° mode cannot be denied when inspecting these figures.

One of the cell's vertical cross-sections can be seen in detail in Fig. 13(c) and the in-plane, temporally-averaged, velocity vectors are superimposed onto the scalar temperature field. Here we see a single elongated roll-cell on the right side of the cross-section with a width approximately equal to the radius of the domain. On the left side of the cross-section two updrafts exist side-by-side. These two updrafts are able to exist in such close proximity because the flow is able to redirect itself toward the cool thermals on either side, thus establishing the spoke-like vortices illustrated in Fig. 11. Virtually all of the flow from the thermal on the far left wall of Fig. 13(c) must contribute to these spoke like structures while the central thermal also contributes toward the roll-cell in the right half of the figure. These two updrafts display signs of a small recirculation region directly between each other, and we suspect that this interaction plays a significant role in perturbing and relocating the central, large-scale thermal. However, further investigation into this phenomenon would require a longer time series.

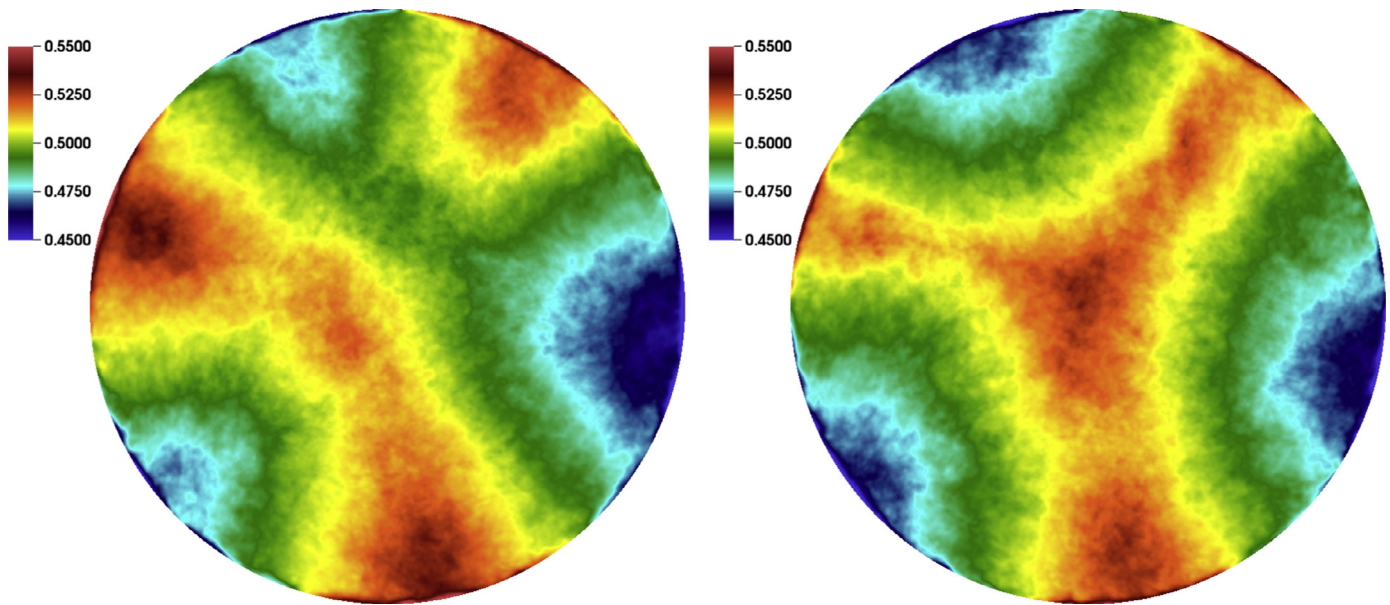


Fig. 10. Temperature field averaged over 0–10 t_ϵ (left) and 10–20 t_ϵ (right) in the $x-y$ plane at $z/h = 0.5$ scaled between 0.45 and 0.55 ΔT .

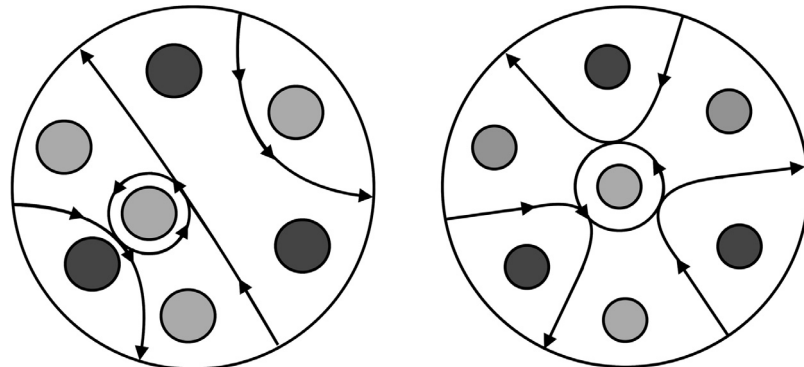


Fig. 11. Conceptual diagrams of the large-scale organization in the flow field averaged over the 0–10 t_ϵ (left) and 10–20 t_ϵ (right). The light circles represent updrafts, the dark circles represent downdrafts and the vectors represent vortex lines.

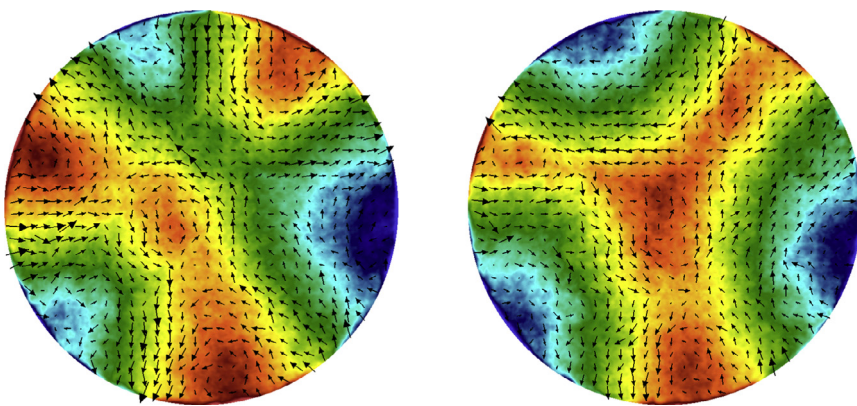


Fig. 12. In plane vorticity plotted on top of temperature in the flow field averaged over the 0–10 t_ϵ (left) and 10–20 t_ϵ (right) in the $x-y$ plane at $z/h = 0.5$ (temperature scaled between 0.45 and 0.55 ΔT , the color panel is the same as in Fig. 10). (For interpretation of the references to color in this figure legend, the reader is referred to the web version of this article).

6. Summary and conclusions

Large scale circulations are known to exist in low aspect-ratio ($\Gamma < 2$) experiments having rectangular and cylindrical shapes (Brown et al., 2005; Zocchi et al., 1990). Experiments and DNS in large aspect ratio domains at Ra above transition (Bailon-

Cuba et al., 2010; du Puits et al., 2007; Xia et al., 2008) have shown that the planform pattern of the convective cells consists of random 3,4,5,6-sided polygons. This DNS study was conducted to explore the structural patterns that characterize RBC in a circular domain of moderate aspect ratio by performing highly resolved simulations in a circular domain of aspect ratio 6.3 at $Pr = 6.7$ and

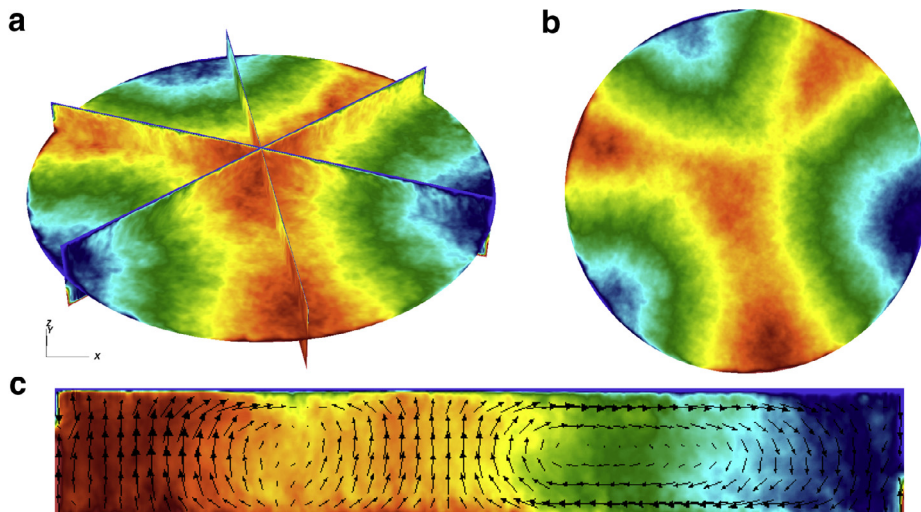


Fig. 13. Images of the temperature field scaled between 0.45 and $0.55\Delta T$ (the color panel is the same as in Fig. 10) averaged over 0 – $20 t_\epsilon$: a horizontal cut plane at $z/h = 0.5$ and vertical cut planes at 40° , 100° , and 160° from the x -axis (a), detailed view of the horizontal cut plane at $z/h = 0.5$ (b), and detailed view of the vertical cut plane 160° from the x -axis with the average, in-plane velocity vectors superimposed (c). (For interpretation of the references to color in this figure legend, the reader is referred to the web version of this article).

$Ra = 9.6 \times 10^7$. The comparison of several resolution criteria in our simulations with the recommended values for RBC confirms that our study is well resolved (Bailon-Cuba et al., 2010; Grötzbach, 1983; Scheel et al., 2013).

The referred geometry and set of parameter values were chosen to allow direct comparison with a PIV experiment (Fernandes, 2001) in which many different states of the convection were sampled over several independent realizations, with at least 100 eddy turnover duration per realization, and in which line averaging and time averaging could be done to improve statistical convergence. In the DNS convergence was improved by averaging over time and horizontal planes. In lieu of the absence of a similar comparison in the previously documented numerical studies of Rayleigh–Bénard convection, the current comparison carries a substantial value. We show that good agreement in temperature and velocity statistics can be obtained between DNS and experimental studies in spite of a large difference in averaging times. In this study we also elucidate on the methodologies allowing for a meaningful comparison between DNS and experimental data obtained with rather different data collection techniques.

Comparison with the experiment confirmed the validity of the DNS with accuracy of 5% for the temperature and vertical velocity statistics when the statistics were averaged over horizontal planes that spanned the entire domain. The velocity field averaged within a central sub-volume was more sensitive, even showing mean vertical velocity of sign opposite to the experiment, indicating an effect of the large scale structures.

The large-scale thermals for this particular configuration organized into a pattern with a high level of symmetry in the azimuthal direction. The pattern of the dominant mode is a 120° periodic arrangement of radially oriented up and down motions caused by roll cells that extend across the depth of the domain. This spoke-shaped pattern of period-three persists over the entire duration of the simulation, 615 free-fall times. These patterns are very similar to the ones observed by Bailon-Cuba et al. (2010) at a similar Γ and Ra despite the difference in Pr .

Instantaneously the spoke pattern is imbedded in small scale turbulence, but still not totally obscured. To extract the spoke pattern from the full turbulent field temporal smoothing over different time-scales was employed. The structure clearly becomes 3 pairs of alternating up and down motions plus a hot rising column in the center of the domain. This pattern persists even after

smoothing over $20 t_\epsilon$, the entire run time of the simulation. The persistence of the azimuthal orientation implies that reorientations of the spokes occur on extremely slow time scales such that in any single experiment or DNS of moderate duration, the underlying circulation biases the results. Moreover, the persistence of the direction of the central column indicated that the pattern does not “flip” during the DNS, a condition that is needed to sample all of the states of the RBC.

Acknowledgments

We would like to acknowledge U.S. National Science Foundation Grants CBET-1335731 and CMMI-1250124, XSEDE allocation TG-ENG140002, and the Arizona State University (2013/2014-MAE-105) Dean's Fellowship for supporting this work.

References

- Adrian, R.J., Ferreira, R.T.D.S., Boberg, T., 1986. Turbulent thermal convection in wide horizontal fluid layers. *Exp. Fluids* 4, 121–141.
- Ahlers, G., Grossmann, S., Lohse, D., 2009. Heat transfer and large scale dynamics in turbulent Rayleigh–Bénard convection. *Rev. Mod. Phys.* 81 (2), 503.
- Bailon-Cuba, J., Emran, M.S., Schumacher, J., 2010. Aspect ratio dependence of heat transfer and large-scale flow in turbulent convection. *J. Fluid Mech.* 655, 152–173. doi:10.1017/S0022112010000820.
- Bodenschatz, E., Pesch, W., Ahlers, G., 2000. Recent developments in Rayleigh–Bénard convection. *Annu. Rev. Fluid Mech.* 32 (1), 709–778.
- Brown, E., Nikolaenko, A., Ahlers, G., 2005. Reorientation of the large-scale circulations in turbulent Rayleigh–Bénard convection. *Phys. Rev. Lett.* 95 (4), 084503.
- Chandra, L., Grötzbach, G., 2008. Analysis and modelling of the turbulent diffusion of turbulent heat fluxes in natural convection. *Int. J. Heat Fluid Flow* 29 (3), 743–751.
- Deardorff, J.W., 1970. Convective velocity and temperature scales for the unstable planetary boundary layer and for Rayleigh convection. *J. Atmos. Sci.* 27 (8), 1211–1213.
- Deville, M.O., Fischer, P.F., Mund, E.H., 2002. *High-order Methods for Incompressible Fluid Flow*, vol. 9. Cambridge University Press.
- Emran, M.S., Schumacher, J., 2015. Large-scale mean patterns in turbulent convection. *J. Fluid Mech.* 776, 96–108. doi:10.1017/jfm.2015.316.
- Fernandes, R.L., 2001. *The Spatial Structure of Turbulent Rayleigh–Bénard Convection*. University of Illinois at Urbana-Champaign, Urbana, IL. (Ph.D. thesis)
- Fischer, P. F., Lottes, J. W., Kherkemeir, S. G., 2015. nek5000 web page, <https://nek5000.mcs.anl.gov/> (accessed 14.05.16.).
- Grötzbach, G., 1983. Spatial resolution requirements for direct numerical simulation of the Rayleigh–Bénard convection. *J. Comput. Phys.* 49 (2), 241–264.
- Kenjeres, S., Hanjalić, K., 1999. Transient analysis of Rayleigh–Bénard convection with a rans model. *Int. J. Heat Fluid Flow* 20 (3), 329–340.
- Kenjeres, S., Hanjalić, K., 2006. Les, t-rans and hybrid simulations of thermal convection at high ra numbers. *Int. J. Heat Fluid Flow* 27 (5), 800–810.

- Kerr, R.M., 1996. Rayleigh number scaling in numerical convection. *J. Fluid Mech.* 310, 139–179.
- du Puits, R., Resagk, C., Thess, A., 2007. Breakdown of wind in turbulent thermal convection. *Phys. Rev. E* 75 (1), 016302.
- Putthenveettil, B.A., Arakeri, J., 2005. Plume strucutre in high Rayleigh-number convection. *J. Fluid Mech.* 542, 217–249.
- Qiu, X.-L., Tong, P., 2001. Large-scale velocity structures in turbulent thermal convection. *Phys. Rev. E* 64 (3), 036304.
- Scheel, J.D., Emran, M.S., Schumacher, J., 2013. Resolving the fine-scale structure in turbulent Rayleigh–Bénard convection. *New J. Phys.* 15 (11), 113063.
- Scheel, J.D., Kim, E., White, K.R., 2012. Thermal and viscous boundary layers in turbulent Rayleigh–Benard convection. *J. Fluid Mech.* 711, 281–305.
- Shelly, M.J., Vinson, M., 1992. Coherent structures on a boundary layer in Rayleigh–Benard turbulence. *Nonlinearity* 5, 323–351.
- Shishkina, O., Thess, A., 2009. Mean temperature profiles in turbulent rayleigh–bénard convection of water. *J. Fluid Mech.* 633, 449–460.
- Shishkina, O., Wagner, C., 2007. Analysis of sheet-like thermal plumes in turbulent Rayleigh–Bénard convection. *J. Fluid Mech.* 599, 383–404.
- Wilson, D., Craft, T., Iacovides, H., 2014. Application of rans turbulence closure models to flows subjected to electromagnetic and buoyancy forces. *Int. J. Heat Fluid Flow* 49, 80–90.
- Xia, K.-Q., Sun, C., Cheung, Y.-H., 2008. Large scale velocity structures in turbulent thermal convection with widely varying aspect ratio. In: Proceedings of the 14th International Symposium on Applications of Laser Techniques to Fluid Mechanics.
- Zimmermann, C., Groll, R., 2015. Computational investigation of thermal boundary layers in a turbulent Rayleigh–Bénard problem. *Int. J. Heat Fluid Flow* 54, 276–291.
- Zocchi, G., Moses, E., Libchaber, A., 1990. Coherent structures in turbulent convection, an experimental study. *Physica A* 166, 387–407.